Front. Earth Sci. 2019, 13(2): 351–360
https://doi.org/10.1007/s11707-018-0733-9

RESEARCH ARTICLE

Comparison of C- and L-band simulated compact polarized SAR in oil spill detection

Xiaochen WANG[1,2,3], Yun SHAO[1,2,3], Fengli ZHANG (✉)[1,2,3], Wei TIAN[1,2,3]

1 Laboratory of Target Microwave Properties, Deqing Academy of Satellite Applications, Huzhou 313200, China
2 Institute of Remote Sensing and Digital Earth, Chinese Academy of Sciences, Beijing 100101, China
3 University of Chinese Academy of Sciences, Beijing 100049, China

Abstract This paper presents the compact polarized (CP) pseudo quad-pol parameters for the detection of marine oil spills and segregation of lookalikes using simulated CP SAR data from full-polarized (FP) SAR imagery. According to the CP theory, 11 polarized parameters generally used for the detection of oil spills were derived from reconstructed pseudo quad-pol data for both C and L bands. In addition, the reconstruction performance between C and L bands was also compared by evaluating the reconstruction accuracy of retrieved polarized parameters. The results show that apart from σ_{HV} and RH, other polarized parameters of σ_{HH}, σ_{VV}, H, α, φ_{H-V}, r, ρ_{H-V}, and γ can be reconstructed with satisfactory accuracy for both C and L bands. Furthermore, C band has a higher reconstruction accuracy than L band, especially for φ_{H-V}. Moreover, the effect of reconstruction of polarized parameters on oil spill classification was also evaluated using the maximum likelihood classification (MLC) method. According to the evaluation of kappa coefficients and mapping accuracy, it is recommended to use σ_{HH}, σ_{VV}, H, ρ_{H-V}, and γ of the C band CP SAR for marine oil spill classification.

Keywords compact polarized, reconstruction, oil spill, classification

1 Introduction

In the past decades, oil leaked from off-shore oil platforms or crude tankers significantly affected the marine ecosystem and coastal environment. Oil spill accidents such as Penglai 19-3 and Dalian 716 that happened in our coastal zone even threatened human health and life safety. As the time of oil spill diffusion and drifting increases, the detrimental effect also increases (Brekke and Solberg, 2005; Solberg, 2012; Fingas and Brown, 2014). Therefore, it is important to detect the occurrence zone of oil spill accidents precisely and as soon as the oil is spilled. Synthetic aperture radar (SAR), an efficient remote sensing tool, has been widely used for marine oil spill detection because of the characteristics of its all-time and all-weather operation mode (Migliaccio et al., 2007; Solberg et al., 2007).

Although the use of SAR is a significant advancement in marine oil spill detection, some problems still need to be solved. Single- or dual-polarized SAR has limited polarized ability for distinguishing oil spill signals from complex sea surface random scattering. Quad-polarized SAR provides abundant polarized information that can significantly improve the detection performance of marine oil spills. However, the main disadvantage of quad-polarized SAR is the narrow swath width. This restricts the application of routine mapping of marine oil spills, causing more difficulty in large-scale sea surface monitoring (Wang et al., 2010; Velotto et al., 2011; Zhang et al., 2015; Zheng et al., 2015).

Compact polarized (CP) SAR, a new type of coherent dual-polarized radar, has been gradually developed as an efficient tool for diverse ocean applications, especially in oil spills and weak-damping lookalike detection (Souyris et al., 2005; Buono et al., 2016). Compared with conventional single- and dual-polarized SAR, CP SAR provides abundant polarized architecture of marine oil spills due to the satellite transmitted power and swath width. In the past decades, CP SAR has been successfully loaded by orbiting satellites. C-band Indian space research organization, Risat-1, equipped with hybrid-polarized (HP) mode CP SAR was launched in 2012. The L-band Japanese aerospace exploration agency, (JAXA) ALOS-

Received May 9, 2018; accepted August 26, 2018

E-mail: zhangfl@radi.ac.cn

PALSAR2, equipped with HP and π/4 mode CP SAR was launched in 2014 (Zhang et al., 2016). CP SAR can be interpreted as a coherent dual-polarized SAR with a larger swath width and higher noise equivalent sigma zero (NESZ). The swath width is guaranteed to be 350 km (the largest swath width for RADASAT-2 standard quad-pol data is 50 km). The NESZ of high-resolution mode RCM is −19 dB. The NESZ of medium-resolution mode RCM is −25 dB (the NESZ of RADARSAT-2 standard quad-pol data is −32 dB), i.e., it is appropriate for large-scale monitoring of oceans. However, because of the absence of calibrated CP SAR data, only simulated CP SAR data can be used in data processing and analysis.

More recently, the significant potential of CP SAR in ocean oil spill detection and identification was revealed with simulated CP SAR data, instead of actual CP SAR data. The capability of HP mode in oil spills and weak-damping lookalike detection were investigated using Risat-1 off the coast of Norway. Besides Stokes parameters, the relative phase, orientation, ellipticity, and polarization angle, four compact decomposition methods derived from CP Stokes parameters, were also applied in the identification of oil spill regions (Kumar et al., 2014). The performance of HP mode, simulated by RADARSAT-2 quad-polarized SAR data covering oil spill experiments outside Norway and the Deepwater Horizon incident in the Gulf of Mexico, was successfully evaluated to detect the oil spill features (Salberg et al., 2014). A new method for distinguishing oil spills from two types of important lookalikes based on the X-Bragg model was proposed and verified using the simulated HP and π/4 CP mode data derived from the SIR-C/X-SAR and RADARSAT-2 quad-polarized data (Yin et al., 2015). The CTLR mode exhibited different sensitivities for slick-free, weakly damped slick-covered, and oil-covered sea surfaces for low-to-moderate wind speeds (Nunziata et al., 2015). Two CP reconstruction algorithms were performed to evaluate the applications of CP SAR in the detection of oil slicks and oil platforms, and an unsupervised classification method using the relative phase was used for oil spill mapping (Zhang et al., 2017). The sensitivity of polarimetric parameters extracted from the CP SAR data was analyzed in terms of both oil spill detection and discrimination from weak-damping lookalikes. The performance of polarimetric properties of the electric field scattered off the observed scene and received at the SAR antenna was considered and interpreted in terms of sea surface scattering with and without oil slicks (Buono et al., 2015). The potential of CP for four RCM SAR modes was investigated for the discrimination between oil spills and lookalikes (Dabboor et al., 2017). The simulated CP image data obtained from UAVSAR L-Band quad-polarized images were explored to calculate an oil–water mixing index, indicating negligible differences between the pseudo-quad and quad-pol data (Collins et al., 2015). Because of the abovementioned issues, in this study, a series of C-band RADADSAT-2 and L-band ALOS-2 quad-polarized SAR images were used to simulate the CP SAR data and further assess their respective ability for oil spill classification based on the derived polarized parameters. The dataset used in this paper is described in Section 2. In Section 3, 11 polarized parameters were retrieved from the reconstructed pseudo quad-pol data for both C- and L-band and further used for unsupervised classification for the optimum oil spill identification. Conclusions are given in Section 4.

2 Methodology and datasets

2.1 Methodology

According to the CP theory, only Ctlr and π/4 modes are discussed in this paper, because of a linear transform relationship between DCP and Ctlr mode causing a similar polarized performance (Shirvany et al., 2012; Touzi and Charbonneau, 2014).

The scattering vector $\vec{\boldsymbol{k}}_{\mathrm{Ctlr}}$ and relevant Hermitian covariance matrix $\boldsymbol{C}_{\mathrm{Ctlr}}$ are as follows:

$$\vec{\boldsymbol{k}}_{\mathrm{Ctlr}} = \frac{[S_{\mathrm{HH}} - iS_{\mathrm{HV}} - iS_{\mathrm{VV}} + S_{\mathrm{HV}}]^{\mathrm{T}}}{2}, \tag{1}$$

$$[\boldsymbol{C}_{\mathrm{Ctlr}}] = \langle \vec{\boldsymbol{k}}_{\mathrm{Ctlr}} \vec{\boldsymbol{k}}^{*\mathrm{T}}_{\mathrm{Ctlr}} \rangle = \frac{1}{2}\begin{bmatrix} \langle |S_{\mathrm{HH}}|^2 \rangle & \langle i(S_{\mathrm{HH}} S^*_{\mathrm{VV}}) \rangle \\ \langle -i(S_{\mathrm{VV}} S^*_{\mathrm{HH}}) \rangle & \langle |S_{\mathrm{VV}}|^2 \rangle \end{bmatrix} + \frac{1}{2}\langle |S_{\mathrm{HV}}|^2 \rangle \begin{bmatrix} 1 & -i \\ i & 1 \end{bmatrix}$$

$$= \frac{1}{2}\begin{bmatrix} -2\Im(\langle S_{\mathrm{HH}} S^*_{\mathrm{HV}} \rangle) & \langle S_{\mathrm{HH}} S^*_{\mathrm{HV}} \rangle + \langle S_{\mathrm{HV}} S^*_{\mathrm{VV}} \rangle \\ \langle S^*_{\mathrm{HH}} S_{\mathrm{HV}} \rangle + \langle S_{\mathrm{VV}} S^*_{\mathrm{HV}} \rangle & 2\Im(\langle S_{\mathrm{VV}} S^*_{\mathrm{HV}} \rangle) \end{bmatrix}, \tag{2}$$

where T represents matrix transpose operations; * represents matrix conjugate operations; $\langle\ \rangle$ represents average operations; $\mathcal{R}$ is the real part of a complex number, $\Im$ is the imaginary part of a complex number; S_{HH}, S_{VV}, S_{HV} are the polarization scattering matrix; H, V are the horizontal or vertical polarized channel, respectively.

The scattering vector $\vec{\boldsymbol{k}}_{\pi/4}$ and relevant Hermitian covariance matrix $\boldsymbol{C}_{\pi/4}$ are as follows:

$$\vec{\boldsymbol{k}}_{\pi/4} = \frac{[S_{\mathrm{HH}} + S_{\mathrm{HV}} S_{\mathrm{VV}} + S_{\mathrm{HV}}]^{\mathrm{T}}}{\sqrt{2}}, \tag{3}$$

$$[\boldsymbol{C}_{\pi/4}] = \langle \vec{\boldsymbol{k}}_{\pi/4}\, \vec{\boldsymbol{k}}^{*\mathrm{T}}_{\pi/4} \rangle = \frac{1}{2}\begin{bmatrix} \langle |S_{\mathrm{HH}}|^2 \rangle & \langle S_{\mathrm{HH}} S^*_{\mathrm{VV}} \rangle \\ \langle S_{\mathrm{VV}} S^*_{\mathrm{HH}} \rangle & \langle |S_{\mathrm{VV}}|^2 \rangle \end{bmatrix} + \frac{1}{2}\langle |S_{\mathrm{HV}}|^2 \rangle \begin{bmatrix} 1 & 1 \\ 1 & 1 \end{bmatrix}$$

$$= \frac{1}{2}\begin{bmatrix} 2\mathcal{R}(\langle S_{\mathrm{HH}} S^*_{\mathrm{HV}} \rangle) & \langle S_{\mathrm{HH}} S^*_{\mathrm{HV}} \rangle + \langle S_{\mathrm{HV}} S^*_{\mathrm{VV}} \rangle \\ \langle S^*_{\mathrm{HH}} S_{\mathrm{HV}} \rangle + \langle S_{\mathrm{VV}} S^*_{\mathrm{HV}} \rangle & 2\mathcal{R}(\langle S_{\mathrm{VV}} S^*_{\mathrm{HV}} \rangle) \end{bmatrix}. \tag{4}$$

The scattering vector $\vec{\boldsymbol{k}}_{\mathrm{FP}}$ and relevant Hermitian covariance matrix $\boldsymbol{C}_{\mathrm{FP}}$ are as follows:

$$\vec{\boldsymbol{k}}_{\mathrm{FP}} = [S_{\mathrm{HH}} \sqrt{2} S_{\mathrm{HV}} S_{\mathrm{VV}}]^{\mathrm{T}}, \tag{5}$$

$$[\boldsymbol{C}_{\mathrm{FP}}] = \langle \vec{\boldsymbol{k}}_{\mathrm{FP}}\, \vec{\boldsymbol{k}}^{*\mathrm{T}}_{\mathrm{FP}} \rangle$$

$$= \begin{bmatrix} \langle |S_{\mathrm{HH}}|^2 \rangle & \sqrt{2}\langle S_{\mathrm{HH}} S^*_{\mathrm{HV}} \rangle & \langle S_{\mathrm{HH}} S^*_{\mathrm{VV}} \rangle \\ \sqrt{2}\langle S^*_{\mathrm{HH}} S_{\mathrm{HV}} \rangle & 2\langle |S_{\mathrm{HV}}|^2 \rangle & \sqrt{2}\langle S_{\mathrm{HV}} S^*_{\mathrm{VV}} \rangle \\ \langle S_{\mathrm{VV}} S^*_{\mathrm{HH}} \rangle & \sqrt{2}\langle S_{\mathrm{VV}} S^*_{\mathrm{HV}} \rangle & \langle |S_{\mathrm{VV}}|^2 \rangle \end{bmatrix}. \tag{6}$$

Notably, both $\boldsymbol{C}_{\mathrm{Ctlr}}$ and $\boldsymbol{C}_{\pi/4}$ have the same style of 2×2 matrix; $\boldsymbol{C}_{\mathrm{FP}}$ is a 3×3 matrix. In $\boldsymbol{C}_{\mathrm{FP}}$, the unknown terms $|S_{\mathrm{HH}}|^2$, $|S_{\mathrm{VV}}|^2$, and $|S_{\mathrm{HV}}|^2$ are real; $S_{\mathrm{HH}}S^*_{\mathrm{HV}}$, $S_{\mathrm{HV}}S^*_{\mathrm{VV}}$, and $S_{\mathrm{HH}}S^*_{\mathrm{VV}}$ are complex. When the $\boldsymbol{C}_{\mathrm{FP}}$ is reconstructed from $\boldsymbol{C}_{\mathrm{Ctlr}}$ or $\boldsymbol{C}_{\pi/4}$, three known measured values obtained from the CP SAR covariance matrix are used to retrieve six unknown terms in $\boldsymbol{C}_{\mathrm{FP}}$. The ill-conditioned equation cannot be solved until another restricted condition is applied to reduce the number of unknown terms during the reconstruction.

Two hypothesizes were applied to reduce the number of unknown terms. The first hypothesis is reflection symmetry, which applies to the complete decorrelation between co-polarized and cross-polarized backscattering as follows:

$$\langle S_{\mathrm{HH}} S^*_{\mathrm{HV}} \rangle = \langle S_{\mathrm{HV}} S^*_{\mathrm{VV}} \rangle = 0. \tag{7}$$

Under the reflection symmetry hypothesis, the number of unknown terms in $\boldsymbol{C}_{\mathrm{FP}}$ is reduced from 6 to 4, and the simplified style of $\boldsymbol{C}_{\mathrm{FP}}$ is:

$$[\boldsymbol{C}_{\mathrm{FP}}] = \begin{bmatrix} \langle |S_{\mathrm{HH}}|^2 \rangle & 0 & \langle S_{\mathrm{HH}} S^*_{\mathrm{VV}} \rangle \\ 0 & 2\langle |S_{\mathrm{HV}}|^2 \rangle & 0 \\ \langle S_{\mathrm{HH}} S^*_{\mathrm{VV}} \rangle & 0 & \langle |S_{\mathrm{VV}}|^2 \rangle \end{bmatrix}. \tag{8}$$

The second hypothesis can be expressed by the relationship between co-polarized and cross-polarized backscattering:

$$\frac{|S_{\mathrm{HV}}|^2}{|S_{\mathrm{HH}}|^2 + |S_{\mathrm{VV}}|^2} \approx \frac{1-\rho_{\mathrm{H-V}}}{N}, \tag{9}$$

where S_{HH}, S_{VV}, S_{HV} are the polarization scattering matrix; H, V are the horizontal or vertical polarized channel, respectively; $\rho_{\mathrm{H-V}}$ is the co-polarized correlation coefficient; and N is the key undetermined parameter.

Two solutions are available to confirm parameters N.

1) Souyris's algorithm

In Souyris' algorithm (Souyris et al., 2005), the undetermined parameter N is directly set as 4, and the pseudo quad-pol data are derived from the CP Hermitian covariance matrix by iterative calculation of the co-polarized correlation coefficient $\rho_{\mathrm{H-V}}$ and cross-polarization power $|S_{\mathrm{HV}}|^2$. It is verified that the reconstruction performance of Souyris' algorithm is suitable for the areas dominated by volume scattering. When applied in the area dominated by surface scattering or double-bounce scattering, the reconstruction performance will be significantly deteriorated.

2) Nord's algorithm

Compared with Souyris, Nord et al. (2009) reset the undetermined parameter N by:

$$N = \frac{(|S_{\mathrm{HH}} - S_{\mathrm{VV}}|^2)}{|S_{\mathrm{HV}}|^2}. \tag{10}$$

The expression of N can be regarded as the ratio of double-bounce backscattering $|S_{\mathrm{HH}} - S_{\mathrm{VV}}|^2$ to volume backscattering $|S_{\mathrm{HV}}|^2$, and it is also noted that the initial input of the iteration process of Nord's algorithm is estimated from the Souyris' results, i.e., the initial value of N in the entire iteration process is still 4. By modifying N, it is verified that the convergence ability of Nord's algorithm is much better than Souyris' in its iteration process.

In this paper, Nord's algorithm was performed to reconstruct the CP pseudo quad-pol data. A flowchart of the reconstruction algorithm is shown in Fig. 1. Notably, the two iteration processes are included in the entire reconstruction and the denominator of N is the $|S_{\mathrm{HV}}|^2$ of the first iteration result. The selected stopping threshold of iteration is 10^{-6}.

2.2 Dataset

Two scenes of quad-polarized SAR data were collected in this study, including C-band RADADSAT-2 and L-band ALOS-PALSAR. The specification of imagery parameters is shown in Table 1, and the location of oil spills is also shown in Fig. 1. Scene 1 was observed in the pollution area

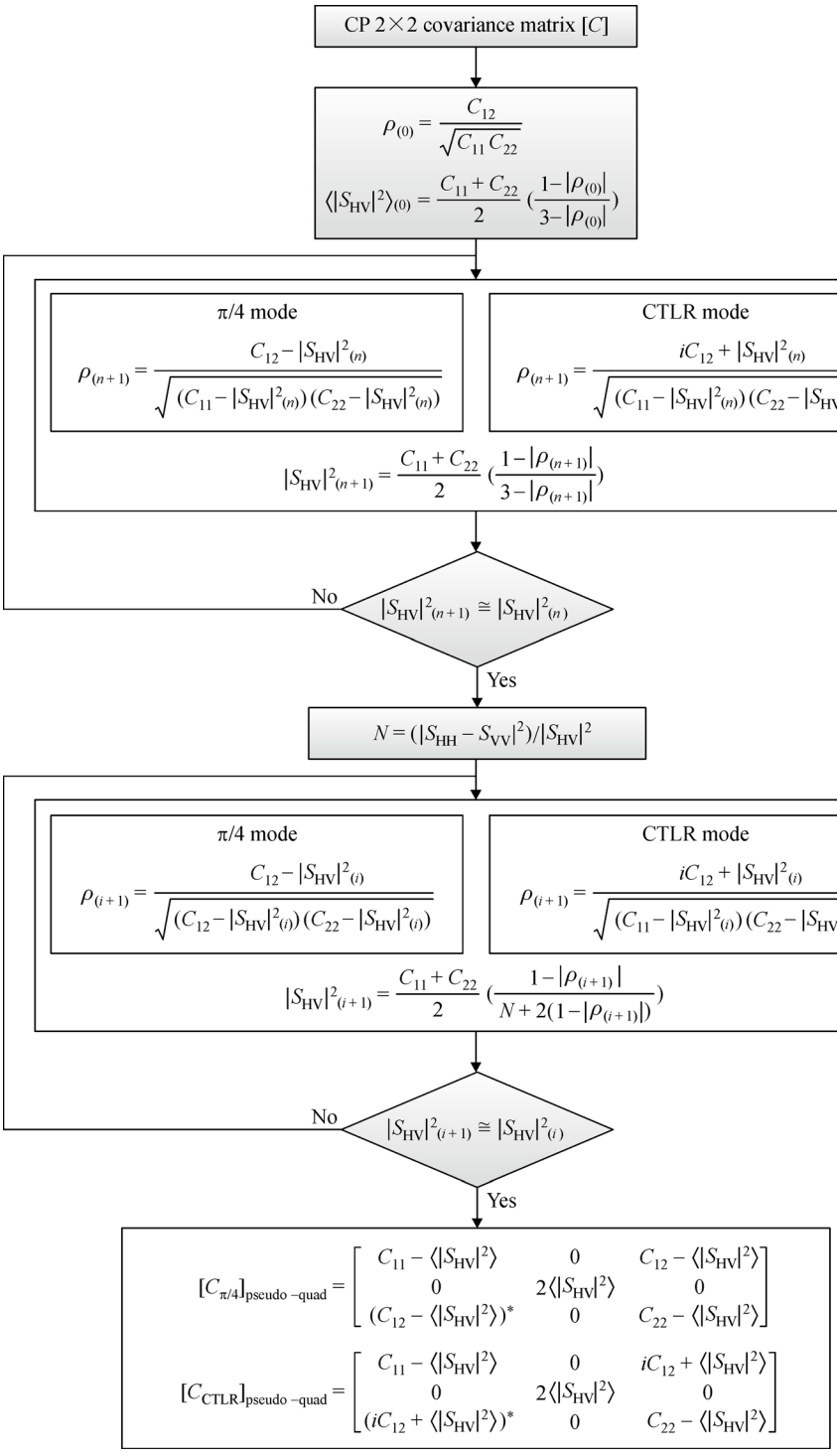

Fig. 1 Flowchart of pseudo quad-pol data reconstruction.

Table 1 Radar parameters of quad-polarized data used for this study

Scene ID	Satellite	Band	Image name	Observation time	Scene position	
					Latitude	Longitude
1	RADADSAT-2	C	RD2016715543-1	07-JUL-2016 06:48	36°00′N	120°45′E
2	ALOS	L	ALPSRP100140730	11-DEC-2007 13:33	36°30′N	126°05′E

from July 7, 2016 in the Yellow Sea of China where parts of oil spills were leaked from unclear sources (Fig. 2(a)). Scene 2 detected oil spill pollution from December 11, 2007 along the northwest coast of Cheonsu bay in South Korea, where heavy oil spills occurred from oil tankers (Fig. 2(b)).

3 Results and discussion

3.1 Comparison of polarized parameters between C- and L-band simulated CP SAR

Prior to efficient detection of oil spills and lookalikes on the ocean surface, polarized parameters should be derived from the reconstructed pseudo quad-polarized data according to Table 2. Eleven polarized parameters were investigated between the C- and L-bands, including three backscattering coefficients of σ_{HH}, σ_{HV}, and σ_{VV}, scattering entropy H, scattering angle α, reference height RH, co-polarized phase difference φ_{H-V}, co-polarized power ratio r, co-polarized correlation ρ_{H-V}, and conformity coefficient γ.

To evaluate the reconstruction performance of polarized parameters on oil spills and lookalikes, reconstruction accuracy was added as the evaluation criterion. This can be expressed as follows:

$$\text{Accuracy} = \frac{Pol_{\text{Ctlr}} - Pol_{\text{FP}}}{Pol_{\text{FP}}}, \tag{11}$$

where Pol_{FP} and Pol_{Ctlr} are the polarized parameters of quad-polarized and Ctlr mode CP SAR, respectively.

The comparison results are shown in Table 3. Here, we also define an empirical threshold of 0.3 as the satisfactory level of accuracy. Notably, apart from σ_{HV} and RH, the other polarized parameters listed in Table 3 can be reconstructed with a satisfactory accuracy for both C and L bands. According to the definition of RH, its low

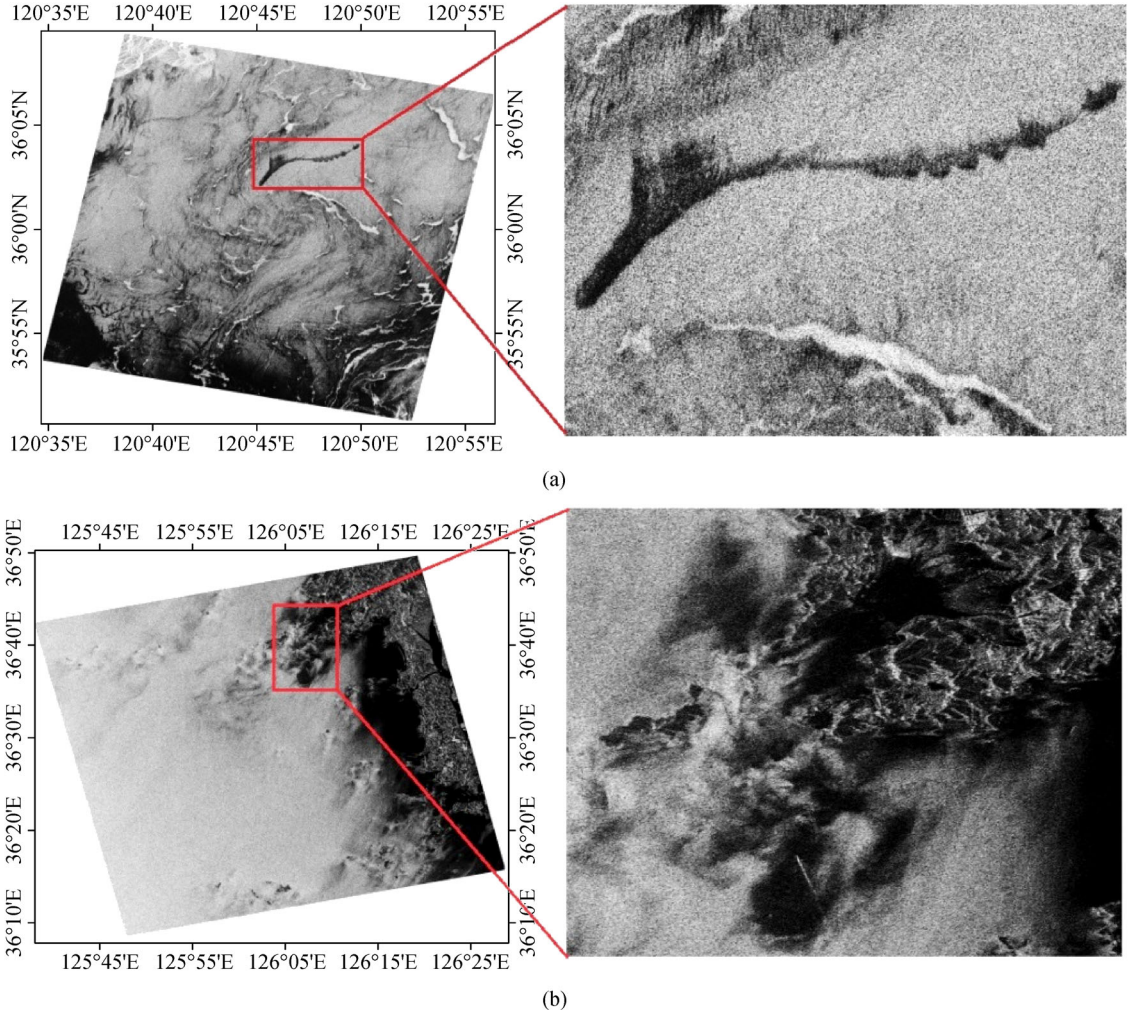

Fig. 2 Location of oil spills and segregation of lookalikes in SAR imagery. (a) C-band RADADSAT-2 quad-polarized SAR imagery, acquisition in 2016-7-7, Yellow Sea, China. (b) L-band ALOS PALSAR quad-polarized SAR imagery, acquisition in 2007-12-11, Cheonsu Bay, South Korea.

Table 2 Polarized parameters used in this paper

Polarized parameters	Definition
Backscattering coefficient	$\sigma^0_{HH} = \langle S_{HH}S^*_{HH}\rangle$, $\sigma^0_{VV} = \langle S_{VV}S^*_{VV}\rangle$, $\sigma^0_{HV} = \langle S_{HV}S^*_{HV}\rangle$
Entropy	$H = \sum_{i=1}^{3} -p_i \log_3 p_i$ ($p_i = \lambda_i / \sum_{j=1}^{3} \lambda_j$), λ_i is the i^{th} eigenvalue of coherency matrix [$\boldsymbol{T}$]
Scattering angle	$\alpha = p_1\alpha_1 + p_2\alpha_2 + p_3\alpha_3$, α_i is derived from the i^{th} eigenvalue of coherency matrix [$\boldsymbol{T}$]
Reference height	$RH = \frac{\lambda_3}{\lambda_1}$
Co-polarized phase difference	$\varphi_{H-V} = \angle\langle S_{HH}S^*_{VV}\rangle$
Co-polarized power ratio	$r = \frac{\langle\lvert S_{HH}\rvert^2\rangle}{\langle\lvert S_{VV}\rvert^2\rangle}$
Co-polarized correlation	$\rho_{H-V} = \lvert\langle S_{HH}S^*_{VV}\rangle\rvert / \lvert S_{HH}\rvert\lvert S_{VV}\rvert$
Conformity coefficient	$\gamma = \frac{2(Re(S_{HH}S^*_{VV}) - \lvert S_{HV}\rvert^2)}{(\lvert S_{HH}\rvert^2 + 2\lvert S_{HV}\rvert^2 + \lvert S_{VV}\rvert^2)}$

Note: S_{HH}, S_{HV}, and S_{VV} are the elements of a Sinclair matrix. $\langle\ \rangle$ represents ensemble average. * represents conjugate operation. *Re* represents the real part.

reconstruction accuracy can be attributed to the low reconstruction accuracy of l_3. This presents the same term of volume scattering with σ_{HV}. In terms of performance of bands, C band has a higher reconstruction accuracy than L band, especially for φ_{H-V}.

Figure 3 shows the scatter plot, detailing how well the reconstructed pseudo quad-pol results fit the original quad-pol data. In Figs. 3(a), 3(b) or 3(e), 3(f), most pixels of scatter points fall close to the one-to-one line with small bias, exhibiting a good reconstruction performance in the HH and VV channels for both C and L bands. However, a large bias in Fig. 3(b) shows the poor reconstruction performance of the HV channel for both C and L bands. On the whole, the performance of C band is better than that of L band. The poor reconstruction accuracy of the HV channel can be attributed to the condition of the reflective asymmetry hypothesis. Because of the effect of sensor noise and the complex scattering mechanism on the ocean surface, $S_{HH}S^*_{HV}$ or $S_{VV}S^*_{VH}$ in the true SAR data is not 0, causing the major bias of the HV channel in reconstruction. In addition, C band seems to perform much better in the reconstruction result. This can be attributed to the fact that C band is much more sensitive to the ocean surface Bragg capillary gravity wave, owing to the nearby scale of wave number.

From the quantitative comparison of listed polarized parameters, the accuracies of all 11 polarized parameters (Table 2) are given in Table 3. In terms of band influence on reconstruction, the reconstruction performance of C band is much more satisfying than that of L band. In terms of polarized parameter influence on reconstruction, the reconstruction results of σ_{HH}, σ_{VV}, H, α, φ_{H-V}, r, ρ_{H-V}, and γ behave well for reconstructed parameter application (accuracy smaller than 10%). Nevertheless, the rest of the parameters do not have a satisfying reconstruction accuracy because of a large bias between the quad-pol and pseudo quad-pol data.

3.2 Effect of polarized parameters on oil-water classification

In this section, the 11 CP parameters were calculated to obtain the oil-water classification. Considering the robustness of the classifier, the method of maximum likelihood classification (MLC) is widely applied in polarized SAR classification (Frost and Yurovsky, 1985; Majd et al., 2012). MLC is a type of classification method based on the Bayesian discriminant function:

$$g_i(x) = p(\omega_i|x) = p(x|\omega_i)p(\omega_i)/p(x), \tag{12}$$

where $p(\omega_i|x)$ is the conditional probability of x in ω_i observation; $p(\omega_i)$ is the prior probability of class type ω_i; $p(x)$ is the occurring probability when x is not about the class type. Assuming that the pixels characteristics of samples conform to a Gaussian distribution, the MLC discriminant criterion can be expressed as follows:

$$g_i(x) = \ln[p(\omega_i)] - \frac{1}{2}\ln|\sum\nolimits_i| - \frac{1}{2}(x-u_i)^{\mathrm{T}}\sum\nolimits_i^{-1}(x-u_i), \tag{13}$$

here x is eigenvector; Σ is covariance matrix.

$$\sum\nolimits_i = \begin{bmatrix} \delta_{11} & \delta_{12} & \cdots & \delta_{1n} \\ \delta_{21} & \delta_{22} & \cdots & \delta_{2n} \\ \vdots & \vdots & \vdots & \vdots \\ \delta_{n1} & \delta_{n2} & \cdots & \delta_{nm} \end{bmatrix}, \tag{14}$$

where $\delta_{ij} = \frac{1}{N}\sum_k (x_{ik} - \mu_i)(x_{jk} - \mu_j)$; x_{ik} is the k^{th} eigenvalue of i^{th} eigenvector; N is the total number of eigenvalues of i^{th} eigenvector; μ_i is the mean vector of i^{th} eigenvector.

Considering the classification performance, 80,000

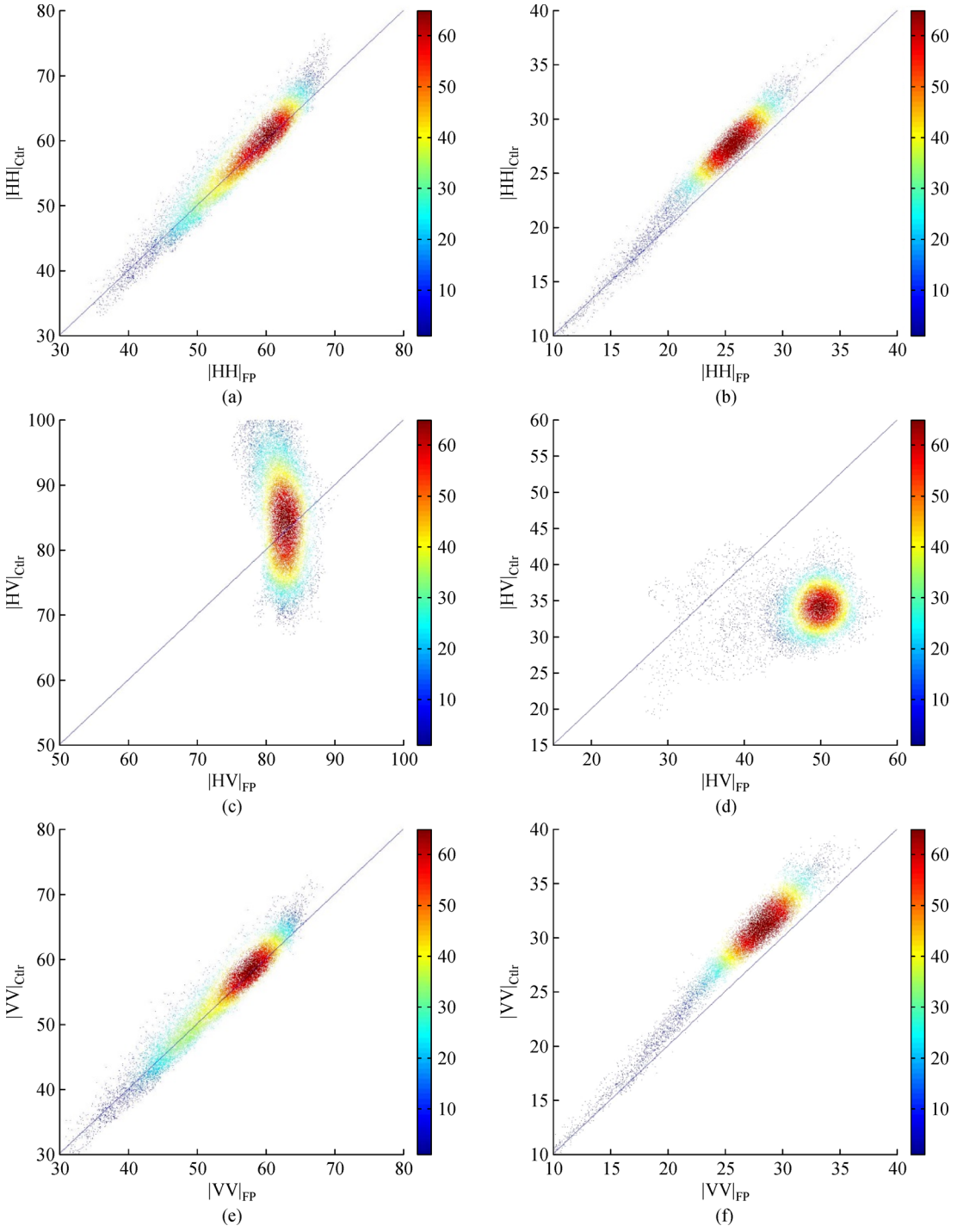

Fig. 3 Reconstruction performance for HH, HV, and VV channels. (a) HH channel of C band; (b) HH channel of L band; (c) HV channel of C band; (d) HV channel of L band; (e) VV channel of C band; (f) VV channel of L band.

pixels were randomly selected as the training input of the classifier, and another 80,000 pixels were used for the verification of classification accuracy. The confusion matrix was derived. Kappa coefficient and mapping accuracy are shown in Table 4.

According to the kappa coefficient and mapping accuracy (Table 4), it was observed that among all the listed polarized parameters, σ_{HH}, σ_{VV}, H, $\rho_{\mathrm{H-V}}$, and γ showed better classification results than the others. For C band, the kappa coefficient of σ_{HH}, σ_{VV}, H, $\rho_{\mathrm{H-V}}$, and γ range from 0.68 to 0.73. For L band, the kappa coefficient of σ_{HH}, σ_{VV}, H, $\rho_{\mathrm{H-V}}$, and γ range from 0.44 to 0.57. Obviously, the classification capability of reconstructed polarized parameters of C band is superior than those of L

Table 3 Comparison of polarized parameters between C- and L-bands

Band	Parameter	Ocean surface features			Average accuracy
		Ocean	Oil spills	Lookalikes	
C	σ_{HH}	0.004	0.056	0.023	0.027
L		0.071	0.106	0.038	0.071
C	σ_{HV}	0.905	1.494	0.765	1.054
L		0.442	6.870	0.555	2.622
C	σ_{VV}	0.006	0.048	0.002	0.056
L		0.075	0.158	0.046	0.093
C	H	0.081	0.227	0.025	0.111
L		0.007	0.437	0.080	0.174
C	α	0.004	0.067	0.013	0.028
L		0.045	0.112	0.021	0.059
C	RH	0.894	2.532	0.636	1.354
L		0.175	10.639	1.092	3.968
C	φ_{H-V}	0.110	0.182	0.324	0.205
L		0.421	0.576	0.834	0.610
C	r	0.034	0.211	0.003	0.086
L		0.149	0.104	0.068	0.107
C	ρ_{H-V}	0.012	0.160	0.034	0.068
L		0.007	0.220	0.004	0.077
C	γ	0.002	0.428	0.012	0.147
L		0.011	0.628	0.008	0.215

Table 4 Classification performance of CP parameters between C- and L-bands

Band	Parameter	Ocean surface features			Kappa coefficient	Mapping accuracy/%
		Ocean	Oil spills	Lookalikes		
C	σ_{HH}	0.0327	0.0027	0.0107	0.6799	80.6
L		2.155	0.1449	0.6838	0.5509	68.4
C	σ_{VV}	0.0445	0.0037	0.0146	0.7028	82.1
L		2.056	0.1344	0.7161	0.5721	70.1
C	H	0.1060	0.6956	0.2192	0.7251	84.4
L		0.1885	0.8340	0.2910	0.4428	63.5
C	α	49.43	54.23	49.26	0.2315	52.1
L		44.44	50.73	45.96	0.2467	48.3
C	φ_{H-V}	0.0243	0.0197	0.1533	0.0917	49.2
L		0.0726	0.0466	0.0056	0.2591	48.9
C	r	0.7374	0.7551	0.7614	0.2364	50.6
L		1.0516	1.0997	0.9635	0.1217	46.1
C	ρ_{H-V}	0.9510	0.4873	0.8803	0.7171	84.1
L		0.9044	0.3761	0.8377	0.4450	63.6
C	γ	0.9360	0.2864	0.8576	0.7313	84.9
L		0.8946	0.1655	0.8205	0.4428	63.6

band. The mapping accuracy also provides similar results as kappa coefficient. Considering the reconstruction accuracy and classification results, we recommend using σ_{HH}, σ_{VV}, H, ρ_{H-V}, and γ of C band for oil spill classification.

As discussed in the reconstruction algorithm, it should be noted that although the reconstruction performance of the HH and VV channels shows satisfying application against quad-pol data, the reconstruction performance of the HV channel should be improved. Because the HV channel exhibiting volume scattering mechanism is significant for many SAR remote sensing retrievals, it is necessary to consider the improvement of HV channel reconstruction, especially for the ocean surface.

4 Conclusions

This paper reveals the potential of CP SAR in marine oil spill detection and classification. Because of the absence of actual CP SAR observation data, two scenes of C-band RADARSAT-2 and L-band ALOS-2 quad-polarized SAR images were used to simulate the CP SAR data. Regarding reconstruction accuracy, apart from σ_{HV} and RH, other polarized parameters of σ_{HH}, σ_{VV}, H, α, φ_{H-V}, r, ρ_{H-V}, and γ can be reconstructed with a satisfactory accuracy for both C and L bands. Furthermore, the polarized parameters with satisfactory accuracies for C band have higher reconstruction accuracies than those for L band, especially for φ_{H-V}. Considering the effect of polarized parameters on oil spill classification, the MLC classification method was also evaluated, and the classification results show that the polarized parameters σ_{HH}, σ_{VV}, H, ρ_{H-V}, and γ exhibit better classification results than others. Moreover, the classification performance of C band is superior to that of L band. Therefore, we recommend to use σ_{HH}, σ_{VV}, H, ρ_{H-V}, and γ of the C band for oil spill classification.

Acknowledgements The authors gratefully acknowledge the financial supports from the National Basic Research Program of China (Nos. 2016YFB0502504 and 2016YFB0502500) and the National Natural Science Foundation of China (Grant Nos. 41431174, 61471358, 41671359, and 41401427), the ALOS research program (PI1404). This article is partly sponsored by the Funding of Scholarship of Chinese Academy of Sciences. The authors would also acknowledge Professor Zhang from the First Institute of Oceanography, State Oceanic Administration, for supporting research on CP theory.

Reference

Brekke C, Solberg A H (2005). Oil spill detection by satellite remote sensing. Remote Sens Environ, 95(1): 1–13

Buono A F, Nunziata M, Migliaccio X, Li X (2016). Polarimetric analysis of compact-polarimetry SAR architectures for sea oil slick observation. IEEE Trans Geosci Remote Sens, 54(10): 5862–5874

Buono A, Nuziata F, Migliaccio M (2015). On the capability of compact-polarimetry SAR architectures to observe oil slicks at sea. In: Proceedings of PolINSAR 2015 Workshop

Collins M J, Denbina M, Minchew B, Jones C E, Holt B (2015). On the use of simulated airborne compact polarimetric SAR for characterizing oil–water mixing of the Deepwater horizon oil spill. IEEE J Sel Top Appl Earth Obs Remote Sens, 8(3): 1062–1077

Dabboor M, Singha S, Topouzelis K, Flett D (2017). Oil spill detection using simulated radarsat constellation mission compact polarimetric SAR data. In: Geoscience and Remote Sensing Symposium

Fingas M, Brown C (2014). Review of oil spill remote sensing. Mar Pollut Bull, 83(1): 9–23

Frost V S, Yurovsky L S (1985). Maximum likelihood classification of synthetic aperture radar imagery. Comput Vis Graph Image Process, 32(3): 291–313

Kumar L J V, Kishore J K, Rao P K (2014). Decomposition methods for detection of oil spills based on RISAT-1 SAR. International Journal of Remote Sensing & Geoscience, 3(4): 1–10

Majd M S, Simonetto E, Polidori L (2012). Maximum likelihood classification of high-resolution SAR images in urban area. Photogramm Fernerkund Geoinf, (4): 395

Migliaccio M, Gambardella A, Tranfaglia M (2007). SAR polarimetry to observe oil spills. IEEE Trans Geosci Remote Sens, 45(2): 506–511

Nord M, Ainsworth T, Lee J, Stacy N J S (2009). Comparison of compact polarimetric synthetic aperture radar modes. IEEE Transactions on Geoscience & Remote Sensing, 47(1): 174–188

Nunziata F, Migliaccio M, Li X (2015). Sea oil slick observation using hybrid-polarity SAR architecture. IEEE J Oceanic Eng, 40(2): 426–440

Salberg A B, Rudjord O, Solberg A H S (2014). Oil spill detection in hybrid-polarimetric SAR images. IEEE Trans Geosci Remote Sens, 52(10): 6521–6533

Shirvany R, Chabert M, Tourneret J Y (2012). Ship and oil-spill detection using the degree of polarization in linear and hybrid/compact dual-pol SAR. IEEE J Sel Top Appl Earth Obs Remote Sens, 5(3): 885–892

Solberg A H S (2012). Remote sensing of ocean oil-spill pollution. Proc IEEE, 100(10): 2931–2945

Solberg A H S, Brekke C, Husoy P O (2007). Oil spill detection in Radarsat and Envisat SAR images. IEEE Trans Geosci Remote Sens, 45(3): 746–755

Souyris J C, Imbo P, Fjortoft R, Mingot S (2005). Compact polarimetry based on symmetry properties of geophysical media: the π/4 mode. IEEE Trans Geosci Remote Sens, 43(3): 634–646

Touzi R, Charbonneau F (2014). Requirements on the calibration of hybrid-compact SAR. In: Geoscience and Remote Sensing Symposium, 1109–1112

Velotto D, Migliaccio M, Nunziata F, Lehner S (2011). Dual-polarized TerraSAR-X data for oil-spill observation. IEEE Trans Geosci Remote Sens, 49(12): 4751–4762

Wang W, Lu F, Wu P, Wang J (2010). Oil spill detection from polarimetric SAR image. International Conference on Signal Processing IEEE, 832–835

Yin J, Yang J, Zhou Z S, Song J (2015). The extended Bragg Scattering model-based method for ship and oil-spill observation using compact polarimetric SAR. IEEE J Sel Top Appl Earth Obs Remote Sens, 8

(8): 3760–3772

Zhang B, Li X, Perrie W, Garcia-Pineda O (2017). Compact polarimetric synthetic aperture radar for marine oil platform and slick detection. IEEE Transactions on Geoscience & Remote Sensing, 55(3): 1407–1423

Zhang X, Zhang J, Liu M, Meng J (2016). Assessment of C-band compact polarimetry SAR for sea ice classification. Acta Oceanol Sin, 35(5): 79–88

Zhang Y, Zhang J, Wang Y, Meng J, Zhang X (2015). The damping model for sea waves covered by oil films of a finite thickness. Acta Oceanol Sin, 34(9): 71–77

Zheng H, Zhang Y, Wang Y (2015). Oil spill detection based on polarimetric feature SERD. Transactions of Oceanology and Limnology, (4): 173−180